This article has been accepted for publication in IEEE Transactions on Power Delivery. This is the author's version which has not been fully edited and content may change prior to final publication. Citation information: DOI 10.1109/TPWRD.2026.3695642



# Application of Impedance-Based Frequency-Dependent System Strength Assessment for Inverter-Dominated Power Systems

Andreas Hadjileonidas, *Graduate Student Member, IEEE,* Deborah Ritzmann, *Member, IEEE,* Pablo Briff, *Senior Member, IEEE,* Peter Davis, Yunjie Gu, *Senior Member, IEEE,* Jonathan Powell, Stefano Lodetti, *Member, IEEE,* Rohit Dambhare, Mark Osborne, Sum Barzegaran, Yue Zhu, *Member, IEEE,* Timothy C. Green, *Fellow, IEEE*

***Abstract*—The increasing penetration of inverter-based resources in Great Britain's power system has resulted in a decline in system strength, which has given rise to sub-synchronous oscillations. Traditional methods of assessing system strength are inadequate for system operators to mitigate these oscillations, and therefore, new system strength assessment methods are needed. This paper presents the design of an end-to-end small-signal system strength monitoring process using online impedance measurements, developed through collaborative efforts of a consortium of industry and research partners. The process is based on the evaluation of frequency-dependent impedances from grid measurement data, followed by the computation of a new small-signal system strength metric, Impedance Margin Ratio. Considerations on the feasibility of a practical implementation of the process in a real-world system subject to measurement uncertainty, along with technical aspects such as the injection configuration, are investigated. The process is validated in electromagnetic transient simulations in PSCAD, on a power system model that resembles a high-inverter-dominated region in Great Britain. The results demonstrate that system strength is highly dependent on operating conditions highlighting the importance of evaluating it across multiple system operating scenarios.**

***Index Terms*—small-signal stability, sub-synchronous oscillations, frequency scan, inverter-based resource, power system measurements.**

## I. Introduction

In an attempt to decarbonise the electricity system in Great Britain (GB) by 2030 [1], renewable energy resources, which are connected to the power system via power electronic inverters, are progressively replacing fossil-fuel-powered synchronous generators. The dynamic behaviour of inverter-based resources (IBR) is shaped by their controller designs, which offer substantial flexibility in their operation but can also introduce unprecedented interactions in the form of oscillations that can disrupt power systems' normal operation. Significant sub-synchronous oscillation events have been observed over the past decade around the world, specifically in regions with large numbers of IBRs. Examples include the 7 Hz voltage oscillations that appeared repeatedly in a high-IBR zone in Australia between 2015-2019 and the 8 Hz voltage oscillations in Scotland in 2021, which reappeared in 2023 [2]. These oscillations, driven by the replacement of synchronous generators by IBRs, reflect a significant system strength decline from a small-signal perspective, which is categorised as the small-signal system strength in [3]. Consequently, online system strength monitoring becomes of vital importance to ensure the stable and uninterrupted operation of power networks, while continuing to introduce more IBRs.

This work was supported in part by network users through the Strategic Innovation Fund (SIF) 10129395, an Ofgem programme managed in partnership with Innovate UK, in part by the Engineering and Physical Sciences Research Council (EPSRC) PhD Studentship EP/W524323/1, in part by Hong Kong JC STEM LAB of Future Energy Systems 2025-0039, and in part by the UK's National Measurement System programme funded by the UK Government's Department for Science, Innovation & Technology (DSIT). (*Corresponding Author: Yue Zhu*).

### A. Review of System Strength Metrics

The traditional system strength metric is the short-circuit ratio (SCR), which is unsuitable for assessing small-signal system strength grids dominated by IBRs, because it is based only on fundamental frequency impedance information and thus fails to capture potential interactions arising from IBRs' wide frequency responses [4]. Variants of SCR such as Weighted SCR, Composite SCR and Equivalent SCR are also assessed at the fundamental frequency and unable to identify the risks of insufficiently damped sub-synchronous oscillations [5]. In light of these shortcomings, a set of frequency-dependent system strength metrics has been recently proposed, which are designed to take into account small-signal interactions among IBRs across a range of frequencies, and are classified as small-signal system strength metrics.

The proposals include the generalised SCR (gSCR) [6], the Grid Strength Impedance Metric (GSIM) [7] and the Impedance Margin Ratio (IMR) [3]. While these novel metrics differ in aspects such as regional granularity, they share a common underlying input quantity, the frequency-dependent whole-system impedance, which is a closed-loop formulation of the grid nodal admittance and impedances of all connected IBRs [8]. Since both the grid nodal admittance and IBR impedances change continuously due to topology changes, control parameter variations and operating point fluctuations [9], online impedance identification is necessary for small-signal system strength monitoring.

This article has been accepted for publication in IEEE Transactions on Power Delivery. This is the author's version which has not been fully edited and content may change prior to final publication. Citation information: DOI 10.1109/TPWRD.2026.3695642



### B. Review of Frequency-dependent Impedance Measurement

The fundamental principle of online impedance identification is to measure the power system's response to a perturbation [10]. Both invasive and non-invasive methods can be employed for online impedance identification. The non-invasive method utilises perturbations that occur naturally in the grid and is also referred to as event data-driven method. The events are typically step changes caused by switching or dispatching, which cause a wide band of harmonic excitation [11], [12]. The key advantage of the non-invasive method is that it does not involve the installation or adaptation of any devices to generate perturbations. However, the timing and characteristics of naturally occurring perturbations cannot be controlled, which limits the availability and accuracy of the impedance measurement results. The invasive method relies on intentionally and periodically introduced perturbations. It requires an injection source at the point of common coupling (PCC) that can be an additional purpose-built asset or an existing grid asset with suitable capabilities such as Flexible AC Transmission (FACTS) devices, HVDC converters and other power converters [13]. The injected signals can be further categorised into narrowband [14] and wideband excitation signals [15]. Since the focus of this work is on implementing online impedance measurement in high-voltage systems and assessing the small-signal system strength from the measurement, narrowband excitation is adopted for its simplicity and high accuracy. This approach is also commonly referred to as a frequency scan or frequency sweep.

### C. Review of High-voltage Measurement

In addition to perturbation injections, frequency scanning also requires precise measurement of voltage and current in high-voltage systems. In a real-world high-voltage network, the three-phase voltage and current data are captured using measurement systems consisting of instrument transformers and digitisation devices, both of which introduce uncertainty to the measurement results. It may be possible to use existing hardware, however, the accuracy of each component of the measurement system must be established to obtain the overall uncertainty in impedance and system strength metric results and assess whether it is acceptable to allow a reliable interpretation for stability assessment. Instrument transformers (also known as transducers) convert voltage and current signals from high-voltage power systems to safe low-amplitude levels as input to measurement, protection or control devices. Ideally, the signal amplitude is stepped down by a nominal ratio, however, the actual ratio will have a deviation defined as the ratio error. Similarly, instrument transformers introduce a shift in the phase angle of the signal, referred to as phase displacement. The IEC 61869 series of standards for voltage transformers and current transformers [16], provides the tolerated ratio error and phase displacement for different accuracy classes solely around the fundamental frequency. The frequency response of phase displacement and ratio error away from the fundamental frequency is more difficult to assess, however some previous work [17] indicates how much the phase displacement and ratio can vary with frequency. For instance, a comparison has demonstrated that some capacitive voltage transformers can have a 20% reduction in ratio by the 5th harmonic (250 Hz for a 50 Hz system) and others may vary by less than 10% ratio at the same the frequency whereas wound voltage transformers demonstrated a substantially lower frequency response on ratio for frequencies up to 300 Hz [18].

### D. Gaps and Contribution

Sections I-A to I-C have reviewed previously developed individual models and methods which are prerequisites for online small-signal system strength assessment. However, to the best of the authors' knowledge, these concepts have not yet been combined to provide an end-to-end process for measurement-driven assessment of frequency-dependent, impedance-based small-signal system strength in high-voltage power systems. Furthermore, to progress towards a real-world physical implementation, there are open questions which have not been fully addressed by previous research, in particular relating to optimal perturbation injection level and selection of frequency scan points, as well as sensitivity to measurement uncertainty.

To address these gaps, a consortium of industry and research partners collaborated within the SYSMET project [19] with the objective to develop and trial solutions for online system strength monitoring by progressing novel theoretical research developments into industrial applications. This paper presents the following contributions from the project:

(i) Design of a detailed end-to-end process for measurement data-driven, frequency-dependent, impedance-based small-signal system strength assessment,
(ii) Analysis of technical considerations for practical implementation, including different perturbation injection levels, frequency scan points and sensitivity to measurement transducer errors,
(iii) Validation of the proposed assessment process using an industry relevant model of a high-voltage power system, in which the recently proposed small-signal system strength metric, IMR, was successfully evaluated. A wide range of grid conditions, including varying short-circuit levels, operating points and network topologies, were thoroughly studied.

The remainder of this article is structured as follows: Section II gives background on the IMR as a candidate system strength metric, Section III describes the design of the online system strength assessment process, Section IV investigates technical considerations for a practical implementation, Section V presents results of applying the stability assessment process to various power system scenarios, and Section VI concludes this article.

## II. Background on Impedance Margin Ratio

### A. Candidate Metric: Impedance Margin Ratio

In this work, IMR has been identified as the candidate metric for small-signal system strength assessment. IMR is a metric that is designed to reflect changes in small-signal stability with the operating point and if evaluated using online admittance measurement it can reduce uncertainties that can arise

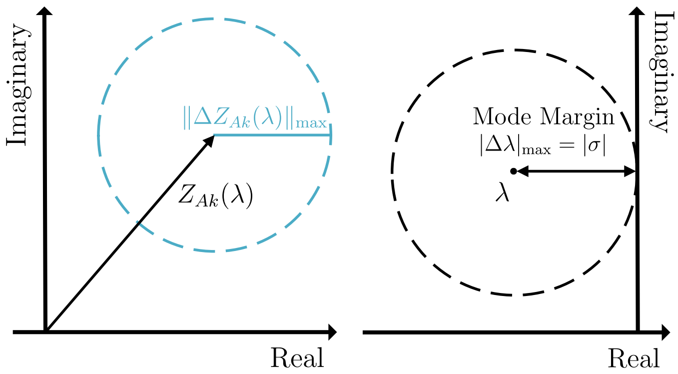


Fig. 1. Impedance Margin Ratio (IMR) interpretation. [3] ©2024 IEEE.

from limited model accuracy. Compared to other frequency-dependent small-signal system strength metrics found in literature, IMR offers several advantages. In particular, compared to the gSCR which only provides a single number to quantify the strength of the whole system, IMR can be calculated for specific locations, revealing variations in local system strength. Additionally, IMR provides a single interpretable value to indicate small-signal strength, whereas GSIM provides values for each point in the frequency spectrum, which then requires interpretation to assess the system strength. A full derivation of IMR can be found in [3], a summary is given in the following paragraphs.

*1) IMR Derivation:* An oscillatory mode $\lambda$ with position $\lambda = \sigma \pm j\omega$ in the complex plane is stable as long as it remains in the left-half complex plane, i.e. $\sigma < 0$. Its maximum allowed change before it becomes unstable is given by the absolute value of its real part, $|\sigma|$, called the mode margin, as shown in the right diagram of Fig.1.

A perturbation to an apparatus' impedance $Z_{Ak}(\lambda)$ connected to bus $k$ will cause a shift to mode $\lambda$ given by [20]:

$$\Delta\lambda = \langle p_{Z_A,\lambda}, \Delta Z_{Ak}\rangle, \tag{1}$$

where $p_{Z_A,\lambda}$ is the impedance participation factor, which reflects the sensitivity of mode $\lambda$ to a change in the apparatus impedance, $\Delta Z_{Ak}$ is the apparatus impedance perturbation at $s = \lambda$ and $\langle\cdot,\cdot\rangle$ is the Frobenius inner product. The impedance participation factor quantifies the level of participation of the apparatus connected at bus-k to the mode $\lambda$. It is defined as the negative residue of the $k$-th diagonal element of the whole system admittance matrix $Y_{kk}^{sys}$: $p_{Z_A,\lambda} = -\text{Res}_\lambda^* Y_{kk}^{sys}$ [20], where $Y^{sys}(s)$ is a frequency domain admittance matrix that incorporates the dynamics of the entire system [8]. The resulting mode shift caused by a perturbation $\Delta Z_{Ak}$ at bus-k is given by:

$$\Delta\lambda = \langle -\text{Res}_\lambda^* Y_{kk}^{sys}, \Delta Z_{Ak}\rangle. \tag{2}$$

The impedance margin, $\|\Delta Z_{Ak}(\lambda)\|_{\max}$, is defined as the maximum allowed change in the impedance of the apparatus, before $\lambda$ moves to the right-half plane. It is obtained by calculating the upper bound of (2) [3]. IMR is the ratio between the impedance margin and the norm of the apparatus impedance evaluated at $s = \lambda$:

$$\text{IMR} = \frac{\|\Delta Z_{Ak}(\lambda)\|_{\max}}{\|Z_{Ak}(\lambda)\|} = \frac{|\sigma|}{\|\text{Res}_\lambda^* Y_{kk}^{sys}\| \cdot \|Z_{Ak}(\lambda)\|}. \tag{3}$$

The normalisation of IMR using the magnitude of local apparatus impedance was designed intentionally with the aim of mitigating the bias toward apparatus rated power and type, and making comparisons across locations directly. This design is also conceptually consistent with the conventional SCR definition, where the short-circuit capacity is normalised by the rated power of the connected apparatus. By normalising the impedance margin $\|\Delta Z_{Ak}(\lambda)\|_{\max}$ with respect to $\|Z_{Ak}(\lambda)\|$, the IMR effectively evaluates the relative sensitivity of the system to changes in the local apparatus, rather than the absolute magnitude of those changes.

*2) IMR Characteristics:* IMR is a small-signal strength metric that can be evaluated at each bus with connected apparatus and for a specific oscillatory mode of the system $\lambda$. Large values of IMR indicate adequate small-signal stability margins at the given location and low sensitivity of the oscillatory mode to changes in the apparatus' impedance. The case studies examined in [3], provide the following system strength interpretations from IMR values:

- IMR $> 0.5$ : Strong
- $0.1 <$ IMR $< 0.5$ : Weak
- $0 <$ IMR $< 0.1$ : Very Weak

The above ranges were empirically derived from case studies in [3], and provide an initial guideline for system strength assessments using IMR. With the wider application of IMR in future system strength studies, these ranges can be progressively refined. It is important to note that IMR, as a small-signal metric, is operating point dependent and therefore should be re-evaluated as system operating conditions change.

### *B. Review of IMR Calculation*

For the calculation of IMR as defined in (3), the following information is required:

- $\lambda = \sigma \pm j\omega$: oscillatory mode of interest,
- $\text{Res}_\lambda^* Y_{kk}^{sys}$: residue of the k-th diagonal element of the whole-system admittance matrix $Y^{sys}$ at $s = \lambda$,
- $Z_{Ak}(\lambda)$: impedance of apparatus connected at bus $k$, evaluated at $s = \lambda$.

The processes of obtaining the required information for the IMR calculation are outlined in the following paragraphs.

*1) Selection of Oscillatory Mode of Interest:* System's oscillatory modes can be obtained from the poles of the parametric model $Y^{sys}(s)$, which are identical to the eigenvalues of the state-space model:

$$\lambda = \text{pole}\ (Y^{sys}) = \sigma \pm j\omega. \tag{4}$$

Among system's oscillatory modes, the most critical ones, i.e. the ones with the smallest damping $|\sigma|$ (closest to the imaginary axis) and smallest damping ratio ($\zeta = \frac{-\sigma}{\sqrt{\sigma^2+\omega^2}}$), are chosen for small-signal strength analysis as they present the highest risk of instability to the system.

This article has been accepted for publication in IEEE Transactions on Power Delivery. This is the author's version which has not been fully edited and content may change prior to final publication. Citation information: DOI 10.1109/TPWRD.2026.3695642



*2) Residue of the Whole-System Admittance Matrix:* As explained in [21], the k-th diagonal element of whole system admittance $Y_{kk}^{sys}(s)$ can be expressed in pole-residue form:

$$Y_{kk}^{sys}(s) = \sum_{i=1}^{m} \frac{R_{ki}}{s - \lambda_i}, \quad (5)$$

where m is the number of poles of the system, and $R_{ki}$ is the residue of $Y_{kk}^{sys}(s)$ that corresponds to $\lambda_i$. It is further shown that the residue $R_{ki}$, can be expressed as:

$$R_{ki} = \text{Res}_{\lambda_i} Y_{kk}^{sys} = \lim_{s \to \lambda_i} (s - \lambda) \cdot Y_{kk}^{sys}(s) = c_k \phi_i \psi_i b_k, \quad (6)$$

where $c_k$ and $b_k$ are the k-th rows and columns, respectively, of the output and input matrices of the state space of $Y^{sys}$, $C$ and $B$, and $\phi_i$ and $\psi_i$ are the right and left eigenvectors that correspond to mode $\lambda_i$. Therefore, when the parametric model $Y_{kk}^{sys}(s)$ is obtained, it is straightforward to calculate $\text{Res}_{\lambda_i} Y_{kk}^{sys}$. A small residue indicates low participation of the apparatus to the mode, hence, a change in the local apparatus does not lead to significant shifts in the mode and consequently the system can be locally strong even if the mode margin is small. Conversely, from the definition of IMR in (3), larger values of $\|\text{Res}_{\lambda_i} Y_{kk}^{sys}\|$ are typically associated with lower IMR values reflecting higher apparatus participation and thus lower system strength. As the analysis focuses on a single PCC, subscript *kk* is omitted for simplicity in the remainder of this paper.

## III. Design of Online System Strength Assessment

A process has been designed for online measurement-driven, impedance-based small-signal system strength assessment by drawing on recently introduced small-signal system strength metrics and by selecting a specific implementation of the frequency scan method to obtain the frequency-dependent impedances. The design choices, rationale and relevant theoretical concepts are presented in this section.

### A. Frequency-Dependent Impedance Measurement

As described in section II-B, the calculation of IMR requires the parametric models of the whole-system admittance $Y^{sys}(s)$ and the apparatus' impedance $Z_A(s)$. Both $Y^{sys}(s)$ and $Z_A(s)$ can vary over time due to changes in grid topology and apparatus' operating conditions. Therefore, to monitor IMR accurately during real-time operation, measurement of frequency-dependent impedance at the grid bus is essential. The main stages of any impedance/admittance measurement procedure are (i) voltage or current perturbation with relevant frequency content, (ii) measurement of power system response to perturbation, and (iii) calculation of frequency-dependent impedance/admittance from measurements. As discussed above, the perturbations could either be invasive or non-invasive and contain a single or multiple frequency components. This paper utilises the conventional frequency scan method using sequential in-series injections of single-tone voltage sine waves. This method is expected to yield high accuracy since a steady voltage perturbation amplitude can be achieved across all frequencies, and there is no spectrum leakage problem. The IMR calculation could also use admittance values identified using a wideband excitation method as long as the same measurement accuracy can be achieved.

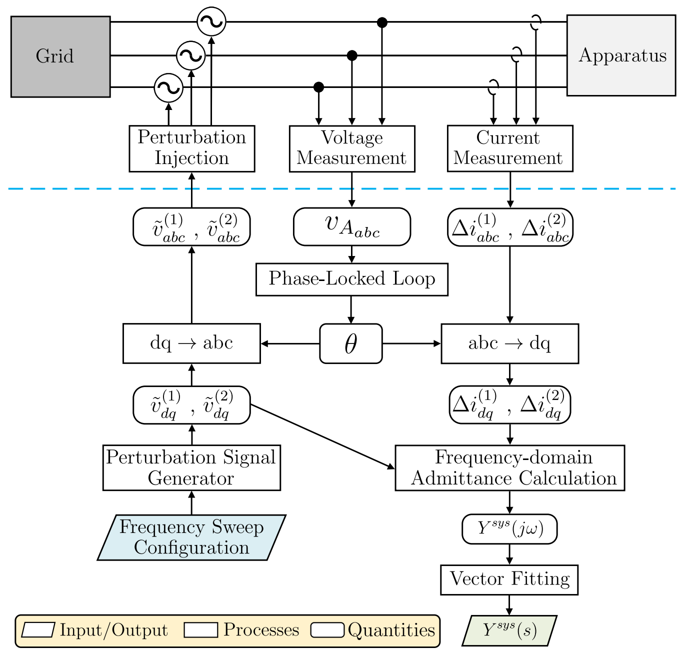


Fig. 2. Schematic overview of frequency scan process.

*1) Measurement of Whole-System Admittance:* Frequency scan has been presented in various previous works such as [14]. Fig. 2 provides a schematic overview of the specific procedure designed and used in this study.

The result of the frequency scan is a discrete spectrum $Y^{sys}(j\omega)$ at frequency points $\omega_i$, from which a parametric admittance model $Y^{sys}(s)$ is identified through vector fitting as described at the end of this section.

The $dq$-frame is selected in this study as it provides a direct relationship with the oscillation phenomena, where the poles of $Y^{sys}$ are the system's oscillatory modes, and aligns with the candidate metric, IMR, which is proposed under the $dq$-frame. The $dq$-frame impedances of the three-phase power electronics devices are coupled because of the time-periodic nature of their dynamics. The impedances/admittances at any given frequency $\omega_i$ in the $dq$-frame, must be represented as a 2 by 2 matrix with non-zero off-diagonal coupling elements. Thus, at each frequency point $\omega_i$, the relationship between the small-signal voltage perturbation $\tilde{v}$, the small-signal current response $\Delta i$ and the whole-system admittance, $Y^{sys}$ is a multiple-input multiple-output (MIMO) model [14]:

$$\begin{bmatrix} Y_{dd}^{sys}(j\omega_i) & Y_{dq}^{sys}(j\omega_i) \\ Y_{qd}^{sys}(j\omega_i) & Y_{qq}^{sys}(j\omega_i) \end{bmatrix} \begin{bmatrix} \tilde{v}_d(j\omega_i) \\ \tilde{v}_q(j\omega_i) \end{bmatrix} = \begin{bmatrix} \Delta i_d(j\omega_i) \\ \Delta i_q(j\omega_i) \end{bmatrix}. \quad (7)$$

The frequency range of interest concerning potential inverter control interactions has been selected as $2\,\text{Hz}$ to $300\,\text{Hz}$ in the $dq$-frame. At each frequency of interest, two sets of linearly independent voltage perturbations are required to identify all admittance values. The first perturbation $\tilde{v}^{(1)}(j\omega_i)$ is configured to have only a d-axis component, while the

This article has been accepted for publication in IEEE Transactions on Power Delivery. This is the author's version which has not been fully edited and content may change prior to final publication. Citation information: DOI 10.1109/TPWRD.2026.3695642



second perturbation $\tilde{v}^{(2)}(j\omega_i)$ only has a q-axis component. Together with the two measured current responses $\Delta i_d^{(1)}, \Delta i_q^{(1)}$ and $\Delta i_d^{(2)}, \Delta i_q^{(2)}$, a fully determined linear system of equations can be formed:

$$\begin{bmatrix} Y_{dd}^{sys} & Y_{dq}^{sys} \\ Y_{qd}^{sys} & Y_{qq}^{sys} \end{bmatrix} \begin{bmatrix} \tilde{v}_d^{(1)} & 0 \\ 0 & \tilde{v}_q^{(2)} \end{bmatrix} = \begin{bmatrix} \Delta i_d^{(1)} & \Delta i_d^{(2)} \\ \Delta i_q^{(1)} & \Delta i_q^{(2)} \end{bmatrix}. \quad (8)$$

This set of equations can be solved via matrix inversion, which yields:

$$Y_{dd}^{sys} = \frac{\Delta i_d^{(1)}}{\tilde{v}_d^{(1)}}, Y_{dq}^{sys} = \frac{\Delta i_d^{(2)}}{\tilde{v}_q^{(2)}}, Y_{qd}^{sys} = \frac{\Delta i_q^{(1)}}{\tilde{v}_d^{(1)}}, Y_{qq}^{sys} = \frac{\Delta i_q^{(2)}}{\tilde{v}_q^{(2)}}.$$

The voltage perturbations and the admittance calculation are defined in the rotating reference frame ($dq$-frame), however, the physical injections and measurements of voltage and current take place in the three-phase $abc$-frame. Therefore, transformations between the two reference frames are required both for the injections and for the measured signals as illustrated in Fig.2. Transformation between $dq$- and $abc$-frames requires tracking of fundamental voltage phase angle $\theta$ using a phase-locked loop (PLL). Previous studies have shown that the PLL bandwidth can significantly influence the accuracy of the measured admittance spectra [22], which would propagate to introduce errors in IMR measurements. It was found that such errors can be mitigated by choosing the bandwidth of the PLL to be below the minimum perturbation frequency such that the PLL acts as a low-pass filter and thus prevents the perturbations from influencing the PLL phase angle estimation. For this reason, in this study the PLL bandwidth is set to 1 Hz which is below the lowest perturbation frequency of 2 Hz. A slow PLL can introduce phase estimation errors in case of fast frequency variations, however, in this study it is assumed that the system fundamental frequency is maintained around 50 Hz and does not vary significantly during the measurement period.

*2) Apparatus Impedance:* The impedance of the apparatus connected to the bus of interest can be calculated using voltage measurements $\tilde{v}_A$ at the side of the apparatus, together with the current response measurements $\Delta i$:

$$\begin{bmatrix} Z_{A dd} & Z_{A dq} \\ Z_{A qd} & Z_{A qq} \end{bmatrix} = \begin{bmatrix} \tilde{v}_{A,d}^{(1)} & \tilde{v}_{A,d}^{(2)} \\ \tilde{v}_{A,q}^{(1)} & \tilde{v}_{A,q}^{(2)} \end{bmatrix} \cdot \begin{bmatrix} \Delta i_d^{(1)} & \Delta i_d^{(2)} \\ \Delta i_q^{(1)} & \Delta i_q^{(2)} \end{bmatrix}^{-1}. \quad (9)$$

*3) Parametric Impedance Model Estimation:* The analytical transfer functions $Y^{sys}(s)$ and $Z_A(s)$ can be estimated from the numerical frequency scan data $Y^{sys}(j\omega)$ and $Z_A(j\omega)$ using a system identification algorithm, called vector fitting [23]. The vector fitting algorithm aims to derive a continuous state-space model from the discrete frequency response data, whose frequency response matches the frequency scan spectra as closely as possible. To achieve a better fitting result, the order of the model can be increased, with a maximum order equal to the number of frequency response points. However, care needs to be taken when increasing the vector fitting order, as a higher order could result in over-fitting, where noise could be falsely identified as system eigenvalues, leading to inaccurate system strength indications. Vector fitting order should be modified based on the obtained impedance/admittance spectra. After applying vector fitting to the calculated admittance $Y^{sys}(j\omega)$ and obtaining the parametric model $Y^{sys}(s)$, the residue $\text{Res}_{\lambda_i} Y^{sys}$ and consequently IMR can be calculated using (4) and (6), respectively. Fig.3 presents a detailed flowchart illustrating the step-by-step procedure for computing IMR from the obtained frequency scan results.

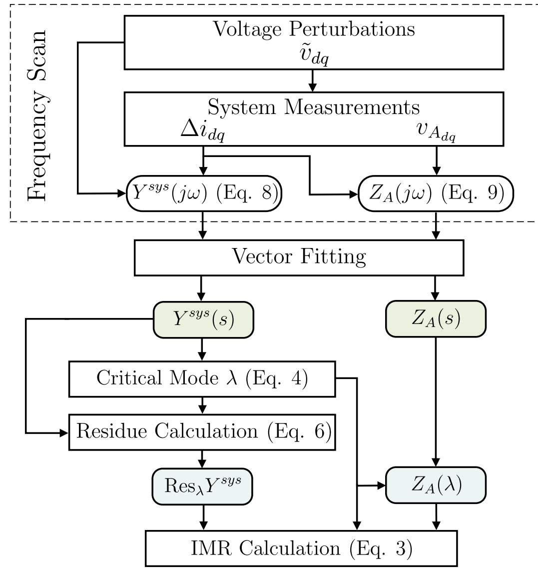


Fig. 3. Flowchart showing the step-by-step calculation of IMR from frequency scan results with the corresponding equation numbers indicated next to each computation step.

## IV. Investigation of Practical Implementation

This section investigates questions that arise on injection parameters and the effects of measurement uncertainties when implementing the system strength assessment process designed in section III. To address these questions, the proposed process for online system strength measurements was implemented and tested in Electromagnetic Transient simulations (EMT) in PSCAD.

### *A. Development of Representative Test System*

The test system used, features an HVDC converter station common in GB, a synchronous condenser and a simple representative distribution network equivalent at the grid-supply point close to the HVDC link. The PSCAD schematic of the test system is shown in Fig. 4. Three controlled voltage sources are connected in series with the main 400 kV transmission line at the PCC of the HVDC converter to provide the required variable frequency voltage perturbations for the frequency scans. The HVDC converter used in this test system is a Modular Multilevel Converter (MMC) based Voltage Source Converter (VSC) HVDC bipole with half-bridge submodule topology. Converter station 1 is set to control the DC-link voltage and either the AC voltage or the reactive power ($Q^{ref}$), and converter station 2 is set to control the active power transfer ($P^{ref}$) of the HVDC link. Positive direction of power flow is considered from the AC system towards the HVDC link. The model is derived from a publicly accessible

This article has been accepted for publication in IEEE Transactions on Power Delivery. This is the author's version which has not been fully edited and content may change prior to final publication. Citation information: DOI 10.1109/TPWRD.2026.3695642



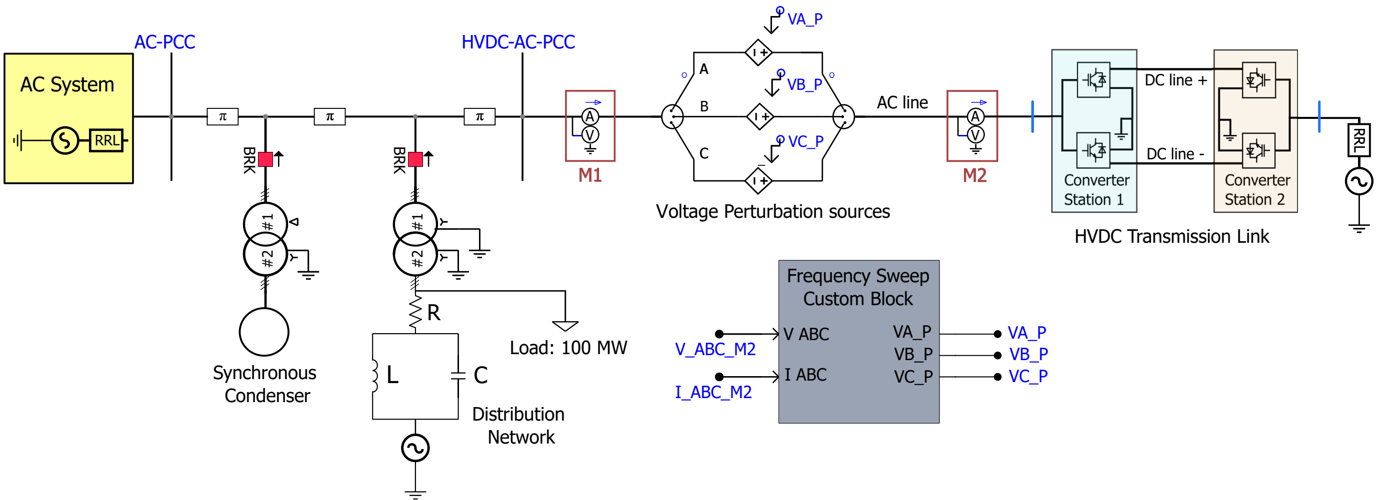


Fig. 4. Schematic of test system used for the simulation studies in PSCAD.

generic model provided by Manitoba Hydro International [24]. The model was modified to feature a converter in a bipole configuration with a total active power rating of $2{,}000\,\mathrm{MW}$ and a $\pm 525\,\mathrm{kV}$ DC link, which reflects the characteristics of the latest HVDC interconnectors within the GB power system. The distribution network is represented by a $132\,\mathrm{kV}$ network consisting of a Thévenin equivalent source, an equivalent $R + L//C$ circuit, and a constant power load of $100\,\mathrm{MW}$. It is connected to the main $400\,\mathrm{kV}$ network through a $260\,\mathrm{MVA}$ $400/132$ kV transformer. The synchronous condenser is based on a generic synchronous condenser model and has a rating of $300\,\mathrm{MVA}$.

A specific PSCAD block was developed in this work, to generate the required voltage perturbation signals and perform the necessary processing on the current response to obtain the frequency-dependent whole-system admittance. The frequency sweep configuration is provided as input to the block, which generates the voltage perturbations in the $dq$-frame. For each frequency of interest, a perturbation is first added to the $d$-axis voltage, followed by a $q$-axis voltage perturbation, to create two sets of linearly independent perturbations allowing the calculation of all four components ($dd$, $dq$, $qd$, and $qq$) of the whole system admittance $Y^{sys}$ as explained in section III-A.

Theoretical ground truth values of oscillatory modes are not available for the HVDC system under study, since it is a complex industrial standard model with some control parts programmed in scripts rather than established in simulation blocks. However, the accuracy of results obtained using the developed impedance scanning block has been verified using other white-box models with theoretically known oscillatory modes, by comparing the fitted results from measured spectra to the analytical models.

### B. Injection Parameters - Frequency Sweep Configuration

*1) Perturbation Amplitude:* The perturbation amplitude must be large enough to be easily detectable from noise or background signals, and at the same time, small enough not to cause any non-linear effects, disturb the operating

TABLE I
RELATIVE ACCURACY METRICS FOR FITTED SYSTEM EVALUATED USING DIFFERENT PERTURBATION SIZES

| Perturbation Size | Root Mean Square Deviation (RMSD) | Normalised Root Mean Square Deviation (NRMSD) | Total Variation |
|---|---|---|---|
| $0.5\% \cdot V^{LL}$ | 0.0034 | 0.036 | 0.483 |
| $1\% \cdot V^{LL}$ | 0.0028 | 0.034 | 0.380 |
| $3\% \cdot V^{LL}$ | 0.0016 | 0.017 | 0.317 |
| $5\% \cdot V^{LL}$ | 0.0015 | 0.015 | 0.294 |

point of the system or cause interference with normal power system operation. To investigate the selection of suitable perturbation amplitude, four different voltage perturbation sizes $[0.5\%, 1\%, 3\%, 5\%] \cdot V_{rated}$ (as a percentage of the rated line-to-line RMS AC voltage, $400\,\mathrm{kV}$) were tested.

While no reference value was available to evaluate the absolute accuracy of the frequency sweep results, a noisy admittance spectrum with many step changes and jumps is considered to be less accurate. Therefore, to evaluate the effect of the voltage perturbation size on the quality of the frequency response results and the vector fitting process results, the discrete frequency scan results $Y^{sys}_{dq}(j\omega_i)$ for each voltage perturbation size are compared with the frequency response of the respective fitted system $Y^{sys-fit}_{dq}(s)|_{s=j\omega_i}$. The frequency response of the fitted system should match the frequency sweep results. To facilitate the comparison, the following metrics are used:

- Root Mean Squared Deviation (RMSD)
  RMSD $=\sqrt{\frac{1}{N}\sum_{i=1}^{N}|Y^{sys}(j\omega_i) - Y^{sys-fit}(j\omega_i)|^2}$,
- Normalised Root Mean Squared Deviation (NRMSD)
  NRMSD $=\sqrt{\frac{1}{N}\sum_{i=1}^{N}\left(\frac{|Y^{sys}(j\omega_i)-Y^{sys-fit}(j\omega_i)|}{|Y^{sys-fit}(j\omega_i)|}\right)^2}$,
- Frequency Scan results Total Variation $=$ $\sum_{i=1}^{N-1}|Y^{sys}(j\omega_{i+1}) - Y^{sys}(j\omega_i)|$,

where $N$ is the number of frequency points, $\omega_i$, used for the frequency scan. Table I shows that as the perturbation size increases, both the RMSD and NRMSD decrease, indicating

This article has been accepted for publication in IEEE Transactions on Power Delivery. This is the author's version which has not been fully edited and content may change prior to final publication. Citation information: DOI 10.1109/TPWRD.2026.3695642



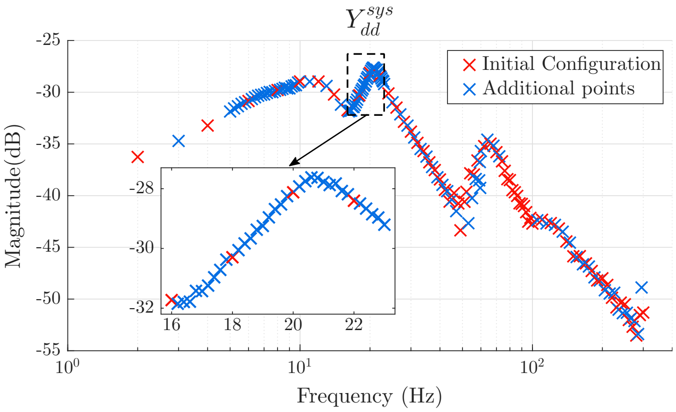


Fig. 5. Bode Plot of $Y_{dd}^{sys}$ showing additional points used for the frequency sweep configuration.

that the frequency response of the fitted system matches the frequency scan results better. Higher Total Variation values at low perturbation sizes suggest larger noise levels and larger jumps in the sweep data that are undesirable and can compromise the system identification process. Therefore, it can be concluded that the largest perturbation sizes tested (3 % and 5 %) yield more accurate results compared to the smaller perturbation sizes.

In the absence of suitable compliance limits for this type of perturbation, the smallest possible amplitude with acceptable accuracy should be chosen. Table I shows that the 3% injections offer a more significant marginal increase in accuracy from the 1% case, compared to the marginal accuracy increase achieved by 5% injections, while causing less disturbance to the network. Therefore, the 3% perturbation size is selected as a compromise between higher accuracy and smaller network disturbance. However, this value may not always be sufficient in real-world conditions, particularly in the presence of measurement noise and other disturbances. A previous study presented a comprehensive methodology for determining the optimal injection magnitude based on noise analysis [25]. In practice, a trial-and-error approach, starting from the recommended 3 %, may be required to identify the most suitable perturbation amplitude for a specific location in the system. It is important to ensure that the small-signal linearity assumption holds for the selected perturbation level. Since these perturbations are expected to be frequently used for impedance measurements in IBR-dominated power systems, further work is needed to establish suitable standards and limits on the maximum permissible level, duration and rate of injections that will prevent interference with normal network operation.

*2) Frequency Sweep Configuration:* The resolution of the impedance/admittance measurements improves as the number of points in the frequency sweep configuration increases. The increased resolution enables the vector fitting algorithm to deliver more accurate results for the system identification, particularly around the spectral peaks. The addition of extra frequency injection points results in an increase in the duration of each frequency scan. There is a trade-off between frequency resolution and frequency scan duration, which should be minimised to reduce risk of interference with normal network operation.

TABLE II
STEP SIZE IN DIFFERENT FREQUENCY RANGES

| Ranges (Hz) | Step Size (Hz) |
|---|---|
| 5-10, 16-23 | 0.2 |
| 2-5, 10-15, 23-49, 51-60 | 1 |
| 60-100 | 2 |
| 100-300 | 5 |

The initial frequency sweep configuration tested consisted of 74 frequency points between 2 Hz to 300 Hz. This frequency range was selected as a representative test case following review of previous studies which vary in the upper limit between 100 Hz and 1,000 Hz [26][27][28]. However, it should be noted that the proposed methodology is applicable to frequencies above 300 Hz. A practical implementation may start with a wider range and as measurement results give insight into the local prevalence of critical modes, the frequency scan range can be reduced to minimise network disturbance from perturbations. After identifying the frequencies where peaks occur in the $Y^{sys}$ spectra (correlated to the system's oscillatory modes), the configuration was modified to increase the point density around the peaks' frequencies, so that the vector fitting algorithm can capture the system's behaviour better near the resonances. Away from these frequencies a larger step size is used as shown in Table II. The Bode plot in Fig. 5 shows the additional points introduced and illustrates, in the inset of Fig. 5, how the peak near 20 Hz in $Y^{sys}$ becomes better defined. It is important to note that points near the 50 Hz frequency in the $dq$-frame are avoided, as those perturbations would result in near-DC or DC component injections in the $abc$-frame, which is problematic. The frequency sweep configuration used in the simulation studies that follow is detailed in Table II. Different frequency point configurations can be used for scans at different system locations depending on the local $Y^{sys}$ characteristics. The results of a preliminary scan can reveal the locations of the spectral peaks, allowing additional frequency points to be introduced in those regions to better capture the spectrum shape.

### C. Baseline Case

The details of the baseline case, used as a reference in the discussion in sections IV-D and V are listed below:

- $P^{ref} = 2{,}000\,\text{MW}$
- AC-PCC Short Circuit Level (SCL) = 10 GVA
- Distribution network connected
- Synchronous Condenser disconnected

From the parametric model, $Y^{sys}(s)$, the system's oscillatory modes are computed using (4) and its pole map is shown in Fig. 6. As discussed in section II-B1, the mode with the lowest damping ratio $\zeta$ and damping $|\sigma|$, $\lambda = -1.99 + 19.82j$ Hz poses the highest instability risk and is thus selected for system strength analysis. An IMR of 0.64 indicates that the system is small-signal strong at the AC bus where the HVDC converter connects (labelled HVDC-AC-PCC) for this operating condition.

This article has been accepted for publication in IEEE Transactions on Power Delivery. This is the author's version which has not been fully edited and content may change prior to final publication. Citation information: DOI 10.1109/TPWRD.2026.3695642



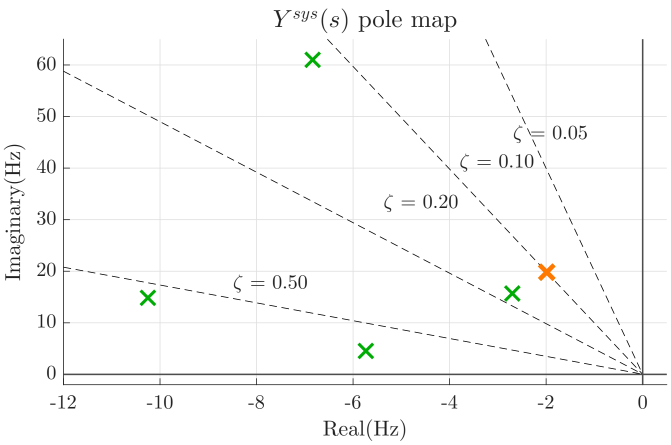


Fig. 6. Pole map of the fitted model $Y^{sys}(s)$ for the baseline case. Dotted lines are constant damping ratio $\zeta$ lines. The orange marker shows the chosen oscillatory mode of interest.

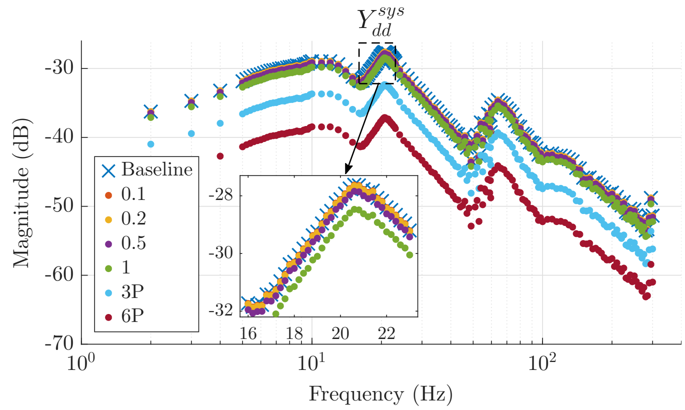


Fig. 7. Bode plots of $|Y_{dd}^{sys}|$ when implementing a gain error (corresponding to different VT accuracy classes) on one of VTs.

TABLE III
TOLERATED RATIO ERROR AND PHASE DISPLACEMENTS FOR VTS

| Accuracy Class | Voltage (ratio) Error (±%) | Phase Displacement (±Centiradians) |
|---|---|---|
| 0.1 | 0.1 | 0.15 |
| 0.2 | 0.2 | 0.3 |
| 0.5 | 0.5 | 0.6 |
| 1 | 1 | 1.2 |
| 3P | 3 | 3.5 |
| 6P | 6 | 7 |

### *D. Non-Ideal Measurements - Voltage Transformer Ratio Error and Phase Displacement*

The baseline admittance and IMR results were calculated using the known theoretical voltage perturbation parameters assuming an ideal injection source. In a realistic scenario, the actual physically injected voltage perturbation may deviate from its configuration, e.g. due to variations in amplitude and phase angle over the injection period. Therefore, the perturbation voltage ($\tilde{v}$) should be calculated from voltage measurements on both sides of the injection source (at measurement points M1 and M2, respectively, as shown in Fig. 4). This section considers two cases of non-ideal voltage transformer (VT) properties influencing the measured voltage perturbation $\tilde{v}$: VT ratio error and VT phase displacement.

In both cases, variations were applied to the ideal voltage waveform measurements taken from the results of the PSCAD simulation baseline case defined in section IV-C. The boundary cases would be if the VTs on both sides have either similar or opposite sign ratio error/phase displacement, whereby the effect on the $\tilde{v}$ measurement would either cancel or reflect the worst-case. As a representative example, one VT was considered to be ideal and the voltage measurements on the other side of the injection source were scaled by the maximum tolerated ratio error or shifted by the maximum phase displacement for the various VT accuracy classes shown in Table III. The modifications were applied to the time domain waveform samples, such that all frequency components were varied by the same gain or shifted by the same phase displacement. The admittance, vector fitting and IMR calculations were then repeated using the non-ideal voltage perturbation measurements. As an initial acceptability threshold, a $5\,\%$ total tolerance on the IMR value is defined to assess the effect of the VT variations.

*1) Effect of Ratio Error:* In Fig. 7, it can be observed that the voltage gain error causes significant shifts in the admittance spectra when varying VT ratio errors for voltage measurements on one side of the injection source, especially for the 3P and 6P protection VT accuracy classes. Fig. 8 shows that the measurement class 1 and the protection transducers 3P and 6P cause shifts in IMR value of $10\,\%$, $74\,\%$ and $199\,\%$, respectively, compared to the baseline case without ratio error. Hence, VTs with unknown ratio errors in these accuracy classes could cause unacceptable deviations in IMR, making the metric unreliable for stability margin assessment. The class 0.5 transducer causes a change of $2.7\,\%$ in IMR compared with the baseline case, this is the lowest accuracy class where the effect of ratio error remains within the desired $5\,\%$ IMR tolerance. However, this could be exceeded once other uncertainties are included. The class 0.1 and 0.2 transducers cause IMR changes of $0.1\,\%$ and $0.5\,\%$ respectively, which would be a more conservative choice to ensure overall accuracy stays within the total tolerance budget of $5\,\%$.

*2) Effect of Phase Displacement:* The result of varying the phase displacement for voltage measurements on one side of the injection source is shown in Fig. 8. Similar to the effect of ratio error, the measurement class 1 and the protection transducers 3P and 6P cause changes in IMR value of $16\,\%$, $97\,\%$ and $252\,\%$ respectively, indicating that these transducer accuracy classes would not be suitable to obtain reliable IMR measurements for stability margin assessment. The 0.5 class transducer causes a change in IMR of $4.4\,\%$ from the baseline case without phase displacement, which would dominate a total tolerance budget of $5\,\%$. This leaves the 0.1 and 0.2 class transducers as more suitable choices since they only cause changes in IMR $0.3\,\%$ and $1.2\,\%$, respectively.

This article has been accepted for publication in IEEE Transactions on Power Delivery. This is the author's version which has not been fully edited and content may change prior to final publication. Citation information: DOI 10.1109/TPWRD.2026.3695642



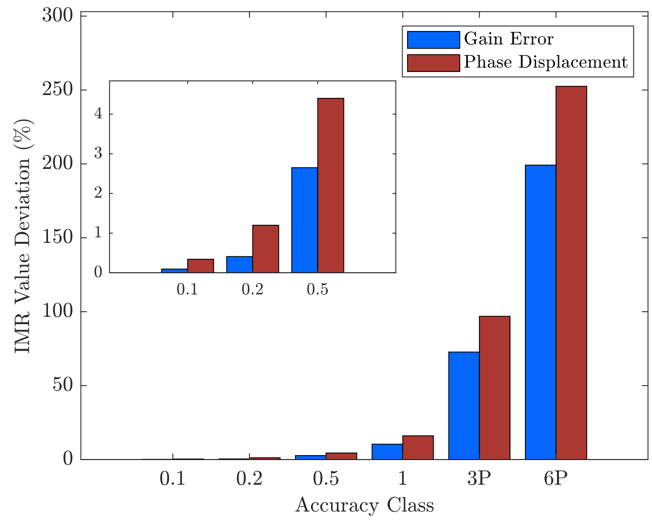


Fig. 8. Percentage deviation in IMR value by implementing a gain error and phase displacement on one of the VTs.

### *E. Further Practical Considerations*

*1) Non-ideal injection source and background noise:* While this section investigates various practical aspects for implementation of the proposed approach for data-driven online small-signal system strength assessment, some assumptions are made. The frequency scan method using sequential in-series injections of single-tone voltage sine waves was selected since it is expected to yield high accuracy as a steady voltage perturbation amplitude can be achieved across all frequencies, and there is no spectrum leakage problem. In practice, the injected perturbation may have some varying deviation from the reference value due to limitations of the injection source. Such variations must be characterised to assess and if necessary mitigate the impact on the resulting IMR measurements. As an alternative to narrowband perturbations, the proposed process could be adapted to utilise controlled wide-band excitation signals consisting of multi-tone sine waves or more complex signals such as a pseudo-random binary sequence, chirp signal or Gaussian pulses. This could improve the capability by increasing the measurement speed of the process since only one injection is necessary instead of multiple sequential injections. However, a limitation of wide-band excitation can be the need for a large overall perturbation magnitude to ensure sufficient signal-to-noise ratio at each frequency component since the accuracy of the admittance measurement depends on the background noise of the power system. The grid noise in previous studies is estimated to approximately 80 dB signal-to-noise ratio [29]. This does not include the presence of harmonics or interharmonics which also need to be considered.

*2) Computational complexity:* The computation of the results in this study indicates that the proposed online identification of the whole system admittance, the extraction of eigenvalues and the IMR calculation from the frequency scan results are not computationally prohibitive for online evaluation. On a standard computer, the IMR computation takes less than 5 s once the frequency scan results are obtained, a duration that could be reduced by software and hardware optimisation. In this work, a vector fitting order of 15 is found to be enough to capture all dominant modes and achieve sufficient accuracy. Increasing the vector fitting order significantly may lead to over-fitting issues and a substantial increase in computational burden, and should therefore be avoided. It is desirable to minimise repeated frequency scans to avoid repeated physical injections into the network. One approach is to trigger the next online system strength assessment only when the operating point has actually changed rather than at pre-defined fixed intervals. A second approach is to build up measurement banks with results for different operating points that can be referenced when the system returns to the same operating conditions. Furthermore, data-driven approaches, such as neural networks and other machine learning techniques can estimate the whole system admittance spectra and IMR values at new operating points based on training from measurements collected at other operating conditions [30].

*3) Application to large-scale power systems:* To demonstrate the application of the proposed methodology in performing local and online system strength assessment, a simple but representative HVDC based system was used. In a practical operational application, the assessment will be implemented in larger power systems with multiple converters. The feasibility of IMR as a system-wide metric has been previously validated in [3] on a modified IEEE 68-bus system using white-box analytical converter models. Demonstration of the proposed end-to-end process on a larger system including comparison of variations between locations is an important validation step, however, this is beyond the scope of this study and is thus recommended for future work.

## V. Results for Variable System Conditions

The investigation of practical technical considerations in the previous section has confirmed the feasibility of the proposed system strength assessment process. The specific configuration of perturbation size and frequency scan points was then used to verify the effectiveness of IMR in reflecting fluctuations in system strength when system configurations and operating conditions change, the results of which are presented in this section. The test cases are categorised into: A) Network changes and B) Operating point changes.

### *A. IMR Sensitivity to Network Changes*

*1) Short Circuit Level Variation:* A reduction in the AC system's SCL is expected to deteriorate system strength. This statement is tested by adjusting the SCL of the host AC system, from 30 GVA to 5 GVA and the corresponding spectra of $|Y_{dd}^{sys}|$ are plotted in Fig.9. To compare changes in the whole system admittance spectrum across different operating conditions, the NRMSD metric as defined in Section IV-B is used to quantify the deviation of $|Y_{dd}^{sys}|$ for SCL values of 5 GVA, 7.5 GVA and 10 GVA relative to the case with SCL = 30 GVA. The results are presented in Table IV and give quantitative confirmation that $|Y_{dd}^{sys}|$ becomes increasingly different as SCL deviates from the SCL = 30 GVA value.

Fig. 9 shows that the peak in the dd-component of the whole system admittance spectrum obtained becomes significantly

This article has been accepted for publication in IEEE Transactions on Power Delivery. This is the author's version which has not been fully edited and content may change prior to final publication. Citation information: DOI 10.1109/TPWRD.2026.3695642



TABLE IV
NRMSD QUANTIFYING THE DEVIATION OF THE $|Y_{dd}^{sys}|$ SPECTRUM FOR DIFFERENT SCL VALUES RELATIVE TO THE CASE WITH SCL = 30 GVA

| **SCL (GVA)** | **10** | **7.5** | **5** |
|---|---|---|---|
| **NRMSD** | 0.344 | 0.434 | 0.855 |

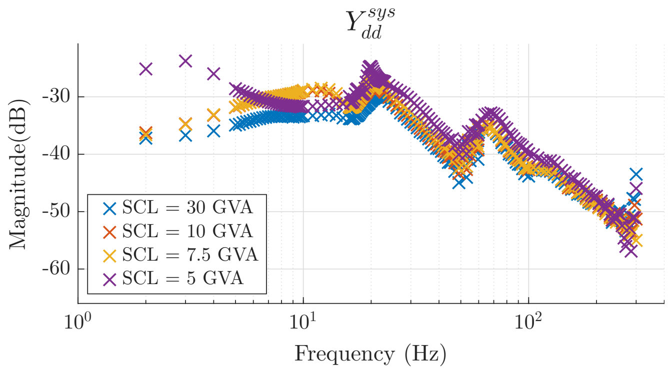


Fig. 9. $|Y_{dd}^{sys}|$ frequency sweep Bode plots for varying AC system's SCL.

sharper and larger in magnitude at the frequency of the oscillatory mode of interest (around 20 Hz), implying a reduction in system strength.

To quantify that, the mode's position throughout the four test cases as well as the corresponding IMR, are calculated and presented in Fig. 10. It is evident that as SCL reduces, IMR decreases, reflecting a decline in the small-signal system strength at the given location. Additionally, the oscillatory mode is shifted towards the right-half plane, closer to instability.

The HVDC link in these case studies is operated at 100 % of its active power rated capacity importing power from the AC system. Among these test cases, only the 5 GVA case results in an IMR indicating a weak system. These system strength assessments can be used to inform system operators' dispatch decisions and procurement of services (such as SCL), to maintain adequate levels of system strength.

*2) Distribution Network Disconnection:* In this test scenario, the distribution network was disconnected from the rest of the system to assess the impact of its frequency-dependent impedance on the transmission network's stability. Such a sensitivity study is conducted to inform transmission owners and system operators of the net contribution of the distribution network to the transmission network's stability margins and help them to address unforeseen and/or planned disconnections at the distribution level. Upon such events, they can modify the demand power setpoints at the transmission level to ensure that the relevant stability margins are maintained.

The distribution network is modelled at the grid supply point (GSP) as an equivalent RLC impedance with a voltage source behind it, and a fundamental-frequency constant power load of 100 MW, representing a realistic operating point in the GB distribution network. The harmonic behaviour of the distribution network at the GSP has been approximated as a high-impedance L-C parallel-resonant circuit, with resonant frequency equal to 9.3 Hz ($abc$-frame), and in series with a 27.5 Ω resistor. Away from that frequency, the distribution network starts to converge to a resistor.

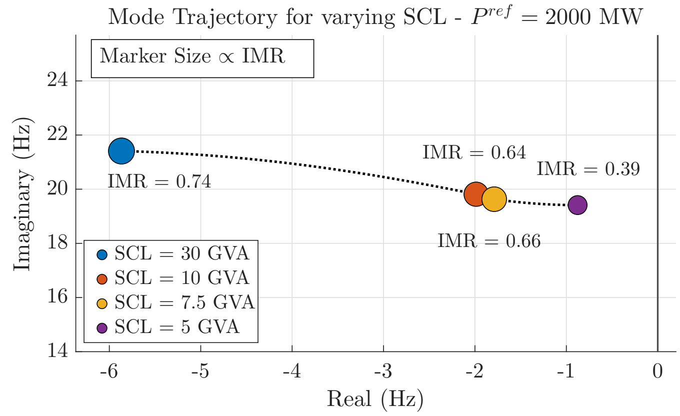


Fig. 10. Oscillatory mode's trajectory and IMR variation as AC system's SCL is changed between 30 GVA and 5 GVA.

TABLE V
SYSTEM STRENGTH CHANGE AS THE DISTRIBUTION NETWORK IS DISCONNECTED

| **Baseline case** | | **Distribution Network Disconnection** | |
|---|---|---|---|
| **Mode (Hz)** | **IMR** | **Mode (Hz)** | **IMR** |
| $-1.99 + 19.82j$ | 0.64 | $-2.41 + 19.23j$ | 0.78 |

The Bode plots presented in Fig. 11 reveal that there is a general reduction in admittance for all frequencies below the resonant peak at 20 Hz after the distribution network disconnection. More significantly, the real part of the critical oscillatory mode becomes slightly more negative, as noted in Table V and the system strength, measured by IMR, improves marginally. This suggests that while the distribution network does participate in the critical oscillatory mode, it does not play a dominant role and there is no significant impact from the 9.3 Hz $abc$-frame resonance point of the L-C circuit.

### B. IMR Sensitivity to Operating Conditions Variations

*1) Active Power Setpoint:* The effect of varying the active power setpoint of the HVDC link on system strength was investigated. In this case study, HVDC converter station 1 is set in $V_{AC}$ control mode, therefore, between different cases, the reactive power output of the HVDC also varies.

Fig. 12 shows the Bode plots of $|Y_{dd}^{sys}|$ for eleven different HVDC loading scenarios ranging from 2,000 MW to −2,000 MW. The frequency response for $P^{ref}$ = 2,000 MW exhibits a large and sharp peak around 20 Hz, indicating high participation of the IBR to an oscillatory mode at that frequency. From the fitted model, the mode is identified as −0.76 + 19.32j Hz and the IMR for that mode is 0.50, as shown in Fig. 13, bringing the system to the edge of being characterised as weak. As the loading decreases from 2,000 MW to 0 MW, the increase in IMR from 0.50 to 0.77, evident from Fig.14, and the corresponding leftward shift of the mode, as seen in Fig.13, reflect a significant system strength improvement.

As the sign of the active power setpoint becomes negative, a substantial change is observed in the shape of $Y^{sys}$ spectra. The peak corresponding to the original mode of interest for

This article has been accepted for publication in IEEE Transactions on Power Delivery. This is the author's version which has not been fully edited and content may change prior to final publication. Citation information: DOI 10.1109/TPWRD.2026.3695642



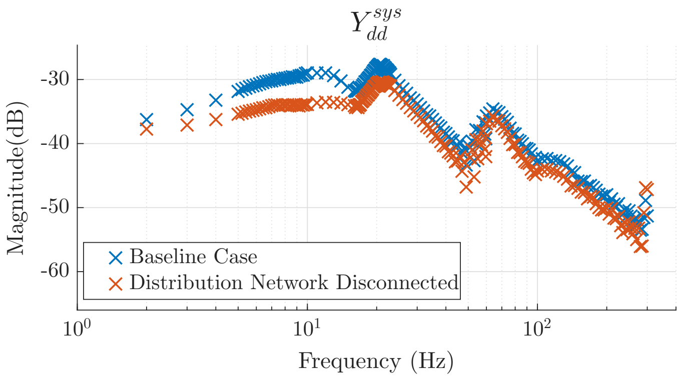


Fig. 11. Bode plots of $|Y_{dd}^{sys}|$ from frequency sweep for baseline case and distribution network disconnection case.

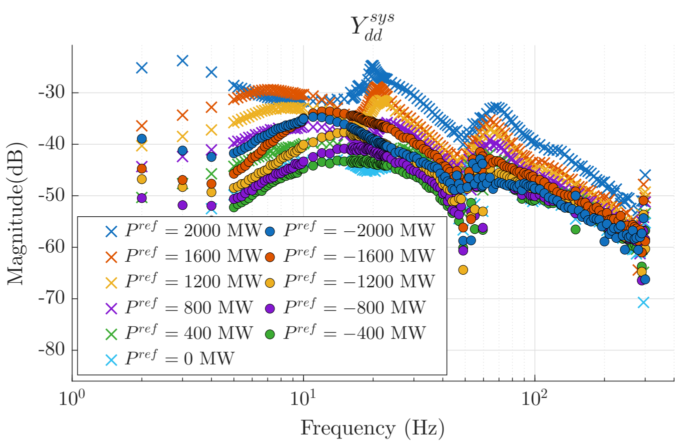


Fig. 12. $|Y_{dd}^{sys}|$ Bode plots for $P^{ref}$ between 2,000 MW and −2,000 MW.

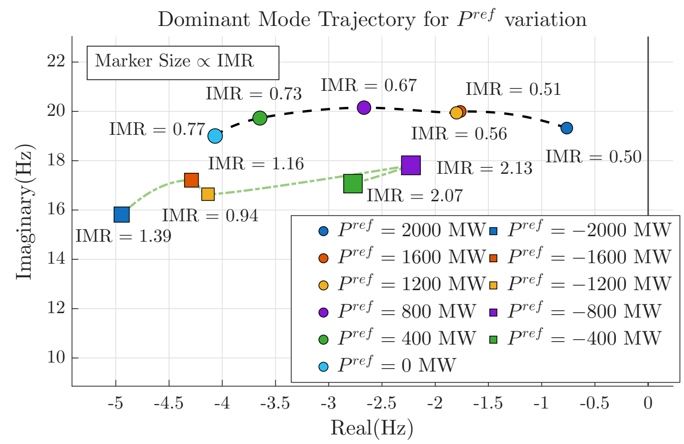


Fig. 13. Trajectory of oscillatory mode with IMR annotation as $P^{ref}$ setpoint is varied from 2,000 MW to −2,000 MW. Different markers show different oscillatory modes picked as the dominant mode.

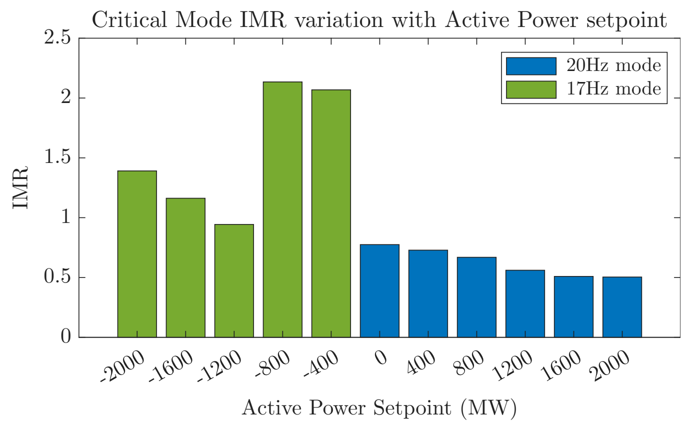


Fig. 14. IMR variation with the active power setpoint of HVDC converter station 2.

positive setpoint cases (≈ 20 Hz) flattens as the power flow is reversed and it is no longer possible to assess system strength with regard to that mode, as the vector fitting algorithm is unable to track it. A lower frequency mode is identified instead (≈ 17 Hz for $P^{ref} = -400$ MW), becoming the 'dominant system mode' used to assess the system strength condition. As shown in a separate trace with square markers in Fig. 13, this mode moves away from the right-half plane (RHP) as the loading increases in the negative direction. Fig.14 highlights that the IMR of this mode is consistently high, reflecting the small sensitivity of the mode to changes in the HVDC as well as the low risk of oscillations associated with that mode.

*2) Reactive Power Setpoint:* The effect of varying the reactive power setpoint of converter station 1 (set in reactive power control mode) on system strength was studied. The setpoint was varied between -1000 MVar and +800 MVar with the active power setpoint set at 1,000 MW.

The Bode plots in Fig. 15 show that when the reactive power setpoint is -1000 MVar, the peak at 20 Hz is the sharpest. As the setpoint changes from negative to positive, it is evident that the peak decreases in magnitude and flattens.

Fig. 16, shows that as the setpoint magnitude decreases from -1000 MVar to 0 MVar, the mode shifts away from the RHP and IMR increases significantly from 0.06 to 0.77. This change reflects an increase in system strength (IMR > 0.5) and a reduction in the risk for oscillatory instability. For positive reactive power setpoints, the mode moves slightly to the right relative to the 0 MVar case, however, IMR increases from 0.77 to 1.30 as shown in Fig.17. The inset of Fig. 16 shows that the oscillatory mode becomes less sensitive to changes in the reactive power setpoint in the positive direction, as it remains largely unchanged as the setpoint increases from +200 MVar to +800 MVar. The reduced sensitivity of the mode to changes in the positive reactive power setpoint is also evident from the significant increase in IMR compared to the 0 MVar case.

In addition to the peak associated with the critical 20 Hz mode, a secondary peak is observed for the −1,000 MVar and −800 MVar cases at approximately 5 Hz. The IMR analysis shows that this mode is located at -1.13 + 4.44j Hz and has an IMR of 0.07 for the −1,000 MVar case and at -1.03 + 5.55j Hz with an IMR of 0.19 for the −800 MVar case. This indicates that at these two operating points, the system is characterised as weak with respect to two distinct modes.

To validate the results of this analysis, a temporary 5% disturbance is applied to the PCC voltage and the time-domain response of the active power at the HVDC converter station 1 is analysed. Fig.18 shows the active power response after the voltage disturbance applied at $t = 6s$. For the −1,000 MVar and −800 MVar cases two dominant oscillatory components

This article has been accepted for publication in IEEE Transactions on Power Delivery. This is the author's version which has not been fully edited and content may change prior to final publication. Citation information: DOI 10.1109/TPWRD.2026.3695642



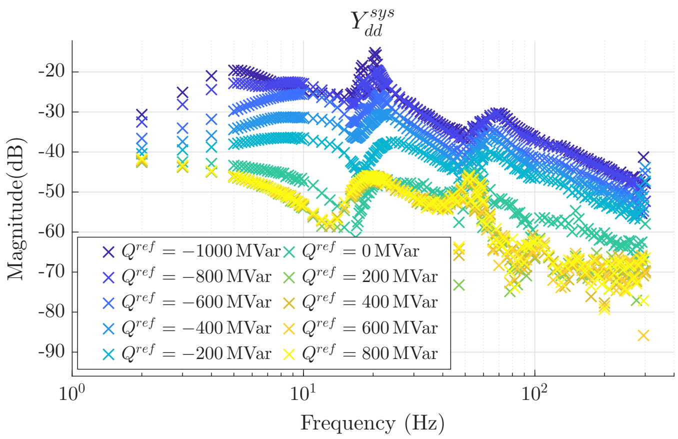


Fig. 15. Bode Plots of the frequency sweep results of $|Y_{dd}^{sys}(j\omega)|$ for various Reactive Power setpoints ($Q^{ref}$) of the HVDC converter station 1.

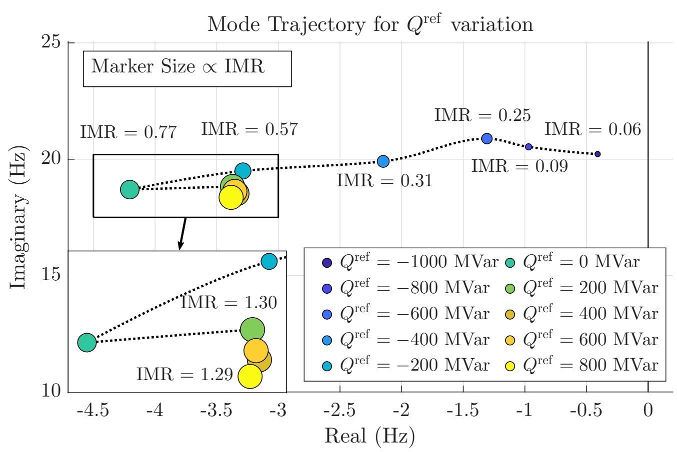


Fig. 16. Trajectory of dominant mode and IMR as reactive power setpoint of HVDC converter station 1 is varied.

are observed at approximately 5 Hz and 20 Hz. The 5 Hz component has a larger initial amplitude compared to the 20 Hz component, which can be attributed to the larger spectral excitation of the lower frequency mode from the step change. As is evident, the 5 Hz oscillation decays relatively fast, as expected from the the damping ratio of the associated mode ($\zeta = 24.6\%$), while in contrast, the 20 Hz mode persists for a significantly longer duration reflecting its lower damping ratio ($\zeta = 2.0\%$) and IMR. These observed oscillations are consistent with the low IMR values calculated for both modes: 0.06 and 0.09 for the 20 Hz mode and 0.07 and 0.19 for the 5 Hz mode for the $-1{,}000$ MVar and $-800$ MVar cases, respectively. Furthermore, it is evident that for the remaining test cases, both the amplitude and duration of the observed oscillations are significantly smaller. These results validate the increase in system strength in these scenarios as reflected by their higher IMR values in Fig.17.

The results of this case study illustrate that a mode's position and system strength do not necessarily change monotonically with variations in the IBR's operating point. Therefore, extrapolating from the results of a small number of operating points would be unreliable, highlighting the need to assess system strength at multiple IBR operating points.

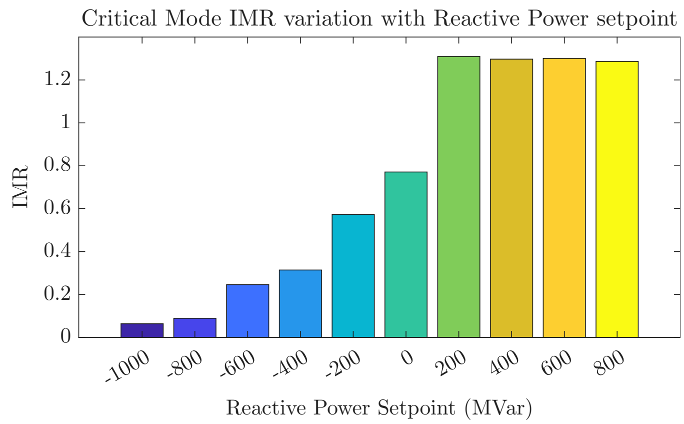


Fig. 17. IMR variation with the reactive power setpoint of the HVDC converter station 1.

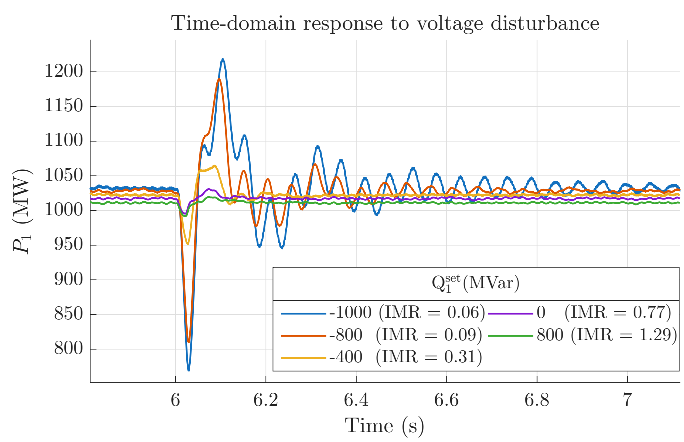


Fig. 18. Response of HVDC converter station 1 active power after temporary PCC voltage disturbance at different reactive power setpoints ($Q_1^{set}$).

## C. Discussion of Results

The objective of the case studies presented in this section was to verify the effectiveness of IMR to reflect changes in small-signal system strength associated with varying system configuration and operating conditions. In some cases the IMR simply confirms the results that would be expected based on classical rules-of-thumb and operator experience. For instance, IMR decreases when SCL is reduced. However, the metric reveals additional useful information: while the significant decrease in SCL from 30 GVA to 7.5 GVA shifts the critical mode significantly towards the right-half plane, the IMR decrease from 0.74 to 0.66 reveals that the small-signal stability state of the system remains strong. In the case of the HVDC active power setpoint variation, the results show very contrasting behaviour for opposite power flow directions. While some of the critical mode locations in the complex plane are relatively close, the IMR indicates very different system stability states. Moreover, the IMR results show that the system strength does not necessarily change monotonically with active or reactive power setpoint or with respect to the mode's distance from the right-half plane. One key strength of the IMR is that it provides a single quantitative output from which system strength can be easily assessed, yet it accounts for the influence of all network components (as reflected by the whole-system admittance) whose complex interaction mechanisms can often not be easily analysed.

## VI. Conclusion

As power systems transition towards very high shares of inverter-based resources, operators are in need of new solutions to monitor small-signal system strength, to mitigate potentially detrimental sub-synchronous oscillations that can lead to significant network disruptions. This article has presented the outcomes of a recent GB collaborative project between industry and researchers, addressing online assessment of system strength. An end-to-end process for a measurement-driven, small-signal system strength assessment method based on impedance spectra, conceived as suitable for real-time monitoring, has been demonstrated in simulation. Technical considerations for practical implementation, including different perturbation injection levels, frequency scan points and sensitivity to transducer measurement errors, have been discussed. A simulation model of a high-voltage power system in PSCAD was used to study impedance margin ratio as a small-signal system strength metric under a range of conditions, including varying short-circuit level, operating points and network topology. The results demonstrate the feasibility and effectiveness of this approach in indicating small-signal system strength and illustrate the importance of evaluating it at multiple credible operating points. This process provides the basis for future implementation of the online system-strength monitoring tool in a real network location.

## Acknowledgments

The authors would like to thank Janet Lees of SSE Renewables for providing advice on industry user requirements for small-signal system strength and frequency-dependent impedance measurement.

## References

[1] Department for Energy Security & Net Zero, "Clean Power 2030 Action Plan: A new era of clean electricity," 2024.

[2] Y. Cheng, L. Fan, J. Rose, S.-H. Huang, J. Schmall, X. Wang, X. Xie, J. Shair, J. R. Ramamurthy, N. Modi, C. Li, C. Wang, S. Shah, B. Pal, Z. Miao, A. Isaacs, J. Mahseredjian, and J. Zhou, "Real-World Subsynchronous Oscillation Events in Power Grids With High Penetrations of Inverter-Based Resources," *IEEE Trans. Power Syst.*, vol. 38, no. 1, pp. 316–330, jan 2023.

[3] Y. Zhu, T. C. Green, X. Zhou, Y. Li, D. Kong, and Y. Gu, "Impedance Margin Ratio: a New Metric for Small-Signal System Strength," *IEEE Trans. Power Syst.*, vol. PP, pp. 1–13, 2024.

[4] H. H. Alhelou, N. Hosseinzadeh, and B. Bahrani, Eds., *Power System Strength: Evaluation methods, best practice, case studies, and applications*. Institution of Engineering and Technology, dec 2023.

[5] B. Badrzadeh and Z. Emin, *Power System Dynamic Modelling and Analysis in Evolving Networks*, ser. CIGRE Green Books. Springer Nature Switzerland, 2024.

[6] F. Ma, H. Xin, D. Wu, and Y. Liu, "Grid Strength Assessment for 100% Inverter-Based Power Systems via Generalized Short-Circuit Ratio Systems," *TechRxiv*, vol. Aug, pp. 0–10, 2023.

[7] C. Henderson, A. Egea-Alvarez, T. Kneuppel, G. Yang, and L. Xu, "Grid Strength Impedance Metric: An Alternative to SCR for Evaluating System Strength in Converter Dominated Systems," *IEEE Trans. Power Del.*, vol. 39, no. 1, pp. 386–396, feb 2024.

[8] Y. Gu, Y. Li, Y. Zhu, and T. C. Green, "Impedance-Based Whole-System Modeling for a Composite Grid via Embedding of Frame Dynamics," *IEEE Trans. Power Syst.*, vol. 36, no. 1, pp. 336–345, 2021.

[9] Y. Wu, H. Wu, L. Cheng, J. Zhou, Z. Zhou, M. Chen, and X. Wang, "Impedance profile prediction for grid-connected vscs with data-driven feature extraction," *IEEE Transactions on Power Electronics*, vol. 40, pp. 3043–3061, 2 2025.

[10] M. K. De Meerendre, E. Prieto-Araujo, K. H. Ahmed, O. Gomis-Bellmunt, L. Xu, and A. Egea-Àlvarez, "Review of local network impedance estimation techniques," *IEEE Access*, vol. 8, pp. 213 647–213 661, 2020.

[11] Z. Wang, L. Bao, L. Fan, Z. Miao, and S. Shah, "From Event Data to Wind Power Plant DQ Admittance and Stability Risk Assessment," *IEEE Trans. Power Syst.*, vol. 37, no. 6, pp. 4400–4408, 2022.

[12] R. Stiegler, J. Meyer, and M. Nazemi, "Measurement and Simulation of Harmonic Propagation in Transmission Systems," in *CIGRE Session*, 2022.

[13] J. Yu, W. Liu, J. Sun, F. Zhang, and Y. Yang, "An improved grid impedance estimator for grid-forming converters in consideration of controller dynamics," *Int. J. Electr. Power Energy Syst.*, vol. 154, p. 109424, dec 2023.

[14] S. Shah, P. Koralewicz, V. Gevorgian, and R. Wallen, "Sequence Impedance Measurement of Utility-Scale Wind Turbines and Inverters - Reference Frame, Frequency Coupling, and MIMO/SISO Forms," *IEEE Trans. Energy Convers.*, vol. 37, no. 1, pp. 75–86, 2022.

[15] A. Riccobono, M. Mirz, and A. Monti, "Noninvasive online parametric identification of three-phase ac power impedances to assess the stability of grid-tied power electronic inverters in lv networks," *IEEE Journal of Emerging and Selected Topics in Power Electronics*, vol. 6, no. 2, pp. 629–647, 2018.

[16] IEC 61869 Series, *Instrument Transformers*, 2011.

[17] H. Seljeseth, E. Saethre, T. Ohnstad, and I. Lien, "Voltage transformer frequency response. Measuring harmonics in Norwegian 300 kV and 132 kV power systems," in *8th International Conference on Harmonics and Quality of Power. Proceedings (Cat. No.98EX227)*, vol. 2. IEEE, 1998, pp. 820–824.

[18] CIGRE Working Group 36-05, "Harmonic, characteristics parameters, methods of study, estimates of existing values in the network," *Electra*, vol. No. 77, 1981.

[19] Energy Networks Association (ENA), "SYSMET – SYstem Strength Measurement and EvaluaTion." [Online]. Available: https://smarter.energynetworks.org/projects/10129395/

[20] Y. Zhu, Y. Gu, Y. Li, and T. Green, "Participation Analysis in Impedance Models: The Grey-Box Approach for Power System Stability," *IEEE Trans. Power Syst.*, vol. 37, no. 1, pp. 343–353, 2022.

[21] Y. Zhu, "Impedance Model Analysis and Measurement for Power System Stability," PhD, Imperial College London, 2022.

[22] H. Gong, D. Yang, and X. Wang, "Impact analysis and mitigation of synchronization dynamics for dq impedance measurement," *IEEE Transactions on Power Electronics*, vol. 34, pp. 8797–8807, 2019.

[23] M. K. Bakhshizadeh, F. Blaabjerg, J. Hjerrild, L. Kocewiak, and C. L. Bak, "Improving the impedance-based stability criterion by using the vector fitting method," *IEEE Trans. Energy Convers.*, vol. 33, no. 4, pp. 1739–1747, 2018.

[24] Manitoba Hydro International, "HVDC VSC transmission interconnecting two AC systems." [Online]. Available: www.pscad.com/knowledge-base/article/222

[25] Y. Zhu, Y. Zhang, and T. C. Green, "Injection Amplitude Guidance for Impedance Measurement in Power Systems," *IEEE Trans. Power Electron.*, vol. 38, no. 6, pp. 6929–6933, 2023.

[26] R. H. Ramakrishna, Z. Miao, and L. Fan, "Stability Analysis of Real-World Subsynchronous Oscillations via Black-Box EMT Models," *IEEE Transactions on Power Delivery*, vol. 39, no. 5, pp. 2855–2867, 2024.

[27] National Energy System Operator (NESO), "Guidance on Oscillation Assessment for Inverter Based Resources (IBRs) - version 2," Tech. Rep., 2025.

[28] L. Fan, Z. Miao, P. Koralewicz, S. Shah, and V. Gevorgian, "Identifying DQ-Domain Admittance Models of a 2.3-MVA Commercial Grid-Following Inverter via Frequency-Domain and Time-Domain Data," *IEEE Trans. Energy Convers.*, vol. 36, no. 3, pp. 2463–2472, 2021.

[29] A. Bhandari, H. Yin, Y. Liu, W. Yao, and L. Zhan, "Real-Time Signal-to-Noise Ratio Estimation by Universal Grid Analyzer," in *2019 International Conference on Smart Grid Synchronized Measurements and Analytics (SGSMA)*. IEEE, may 2019, pp. 1–6.

[30] M. Zhang, X. Wang, D. Yang, and M. G. Christensen, "Artificial neural network based identification of multi-operating-point impedance model," *IEEE Transactions on Power Electronics*, vol. 36, no. 2, pp. 1231–1235, 2021.